

## RESEARCH ARTICLE

View Article Online  
View Journal | View IssueCite this: *Mater. Chem. Front.*,  
2024, 8, 2439Local protons enhance photocatalytic CO<sub>2</sub> reduction by porphyrinic zirconium-organic frameworks†Xue Zhao,<sup>a</sup> Chang-Yan Zhu,<sup>b</sup> Jun-Sheng Qin,<sup>id</sup>\*<sup>ac</sup> Heng Rao,<sup>id</sup><sup>ac</sup>  
Dong-Ying Du,<sup>id</sup><sup>b</sup> Min Zhang,<sup>id</sup>\*<sup>b</sup> Ping She,<sup>id</sup><sup>ac</sup> Li Li<sup>a</sup> and Zhong-Min Su<sup>\*a</sup>

The immobilization of molecular catalysts based on porphyrin fragments within metal-organic frameworks (MOFs) offers a promising approach for achieving sustainable and stable photocatalytic activity. In this study, we presented the synthesis of a phenolic hydroxy-modified iron-porphyrinic zirconium-based MOF, Zr<sub>6</sub>O<sub>4</sub>(OH)<sub>4</sub>(FeTCBPP-OH)<sub>3</sub>, named **MOF-OH** (FeTCBPP-OH = iron 5,10,15,20-tetrakis[4-(4'-carboxyphenyl)-2,6-dihydroxyphenyl]porphyrin), through post-synthetic modification of a precursor MOF called **MOF-OCH<sub>3</sub>** (Zr<sub>6</sub>O<sub>4</sub>(OH)<sub>4</sub>(FeTCBPP-OCH<sub>3</sub>)<sub>3</sub>, FeTCBPP-OCH<sub>3</sub> = iron 5,10,15,20-tetrakis[4-(4'-carboxyphenyl)-2,6-dimethoxyphenyl]porphyrin). Initially, we attempted the direct assembly of Zr<sup>4+</sup> centers and FeTCBPP-OH ligands; however, this approach was unsuccessful in obtaining **MOF-OH**. This perhaps resulted from the high number of hydroxyl groups on the polyphenolic porphyrinic fragments, which exhibited a stronger binding affinity towards zirconium centers. Consequently, we achieved **MOF-OH** by selectively modifying the partial methoxy positions of the FeTCBPP-OCH<sub>3</sub> fragments in **MOF-OCH<sub>3</sub>** through demethylation. To evaluate the photocatalytic performance of **MOF-OH**, we conducted CO<sub>2</sub> reduction experiments without any additional photosensitizer. Remarkably, after 72 hours, the yield of CO reached a high value of 26.8 mmol g<sup>-1</sup>. Notably, the CO production of **MOF-OH** was significantly higher than that of **MOF-OCH<sub>3</sub>**, possibly due to the presence of phenolic hydroxyl substituents, which led to higher local proton concentrations. Furthermore, **MOF-OH** exhibited excellent stability, as demonstrated by the consistent CO production observed during four consecutive runs of CO<sub>2</sub> reduction. To gain insights into the photocatalytic CO<sub>2</sub> reduction process, we conducted a comprehensive series of characterizations and density functional theory calculations, which provided a deeper understanding of the mechanism involved.

Received 8th March 2024,  
Accepted 16th April 2024

DOI: 10.1039/d4qm00187g

rsc.li/frontiers-materials

## Introduction

The conversion of CO<sub>2</sub> into high-energy C1 products has the potential to reduce atmospheric CO<sub>2</sub> levels while enabling sustainable strategies for obtaining valuable chemicals such as CO, HCOOH, CH<sub>3</sub>OH, and CH<sub>4</sub>.<sup>1–3</sup> One promising pathway for this conversion is the photochemical reduction of CO<sub>2</sub>, which utilizes light instead of electricity. Sunlight, an abundant and free energy source, makes this approach particularly attractive.<sup>4,5</sup> Researchers have dedicated considerable efforts

to exploring photocatalysts capable of capturing and reducing CO<sub>2</sub>. In the past few decades, various homogeneous catalysts, including transition metal complexes,<sup>6</sup> ionic liquids,<sup>7</sup> and organocatalysts,<sup>8</sup> have been employed for CO<sub>2</sub> reduction. However, challenges related to catalyst recovery and product separation need to be overcome. Heterogeneous catalysts, such as TiO<sub>2</sub>-based systems<sup>9</sup> and metal-doped zeolites,<sup>10</sup> have been developed, but their practical applications were limited by the high cost of noble metal catalysts. CO<sub>2</sub> can be reduced to CO through a two-electron and two-proton transfer reaction.<sup>11–13</sup> However, CO<sub>2</sub> is a highly stable molecule as it represents the most oxidized state of carbon, requiring considerable energy input for its transformation.<sup>14</sup> Comparatively, photocatalytic systems based on non-precious metal photosensitizers and catalysts hold promise for large-scale applications. Therefore, it is particularly attractive to explore efficient and highly selective photocatalytic systems for CO<sub>2</sub> reduction.<sup>15,16</sup>

Homogeneous catalysts, such as iron tetraphenylporphyrin and its derivatives, have been used for CO<sub>2</sub> photoreduction and have demonstrated high catalytic activities and selectivities.<sup>17,18</sup>

<sup>a</sup> State Key Laboratory of Inorganic Synthesis and Preparative Chemistry, Jilin University, Changchun 130012, P. R. China. E-mail: qin@jlu.edu.cn, suzhongmin@jlu.edu.cn

<sup>b</sup> Department of Chemistry, Northeast Normal University, Changchun 130024, P. R. China. E-mail: mzhang@nenu.edu.cn

<sup>c</sup> International Center of Future Science, Jilin University, Changchun 130012, P. R. China

† Electronic supplementary information (ESI) available: Experimental details, computational details and figures. See DOI: <https://doi.org/10.1039/d4qm00187g>

This can be attributed to the favourable binding of metal active sites with CO<sub>2</sub> and the homogeneity of the photocatalytic systems.<sup>19</sup> Recent studies have shown that hydroxyl functionalization of the macrocyclic benzene ring greatly enhances the selectivity and redox catalytic activity for CO<sub>2</sub> reduction to CO.<sup>20–22</sup> The hydroxyl substituents in the second coordination sphere near the catalytic centres can increase the local proton concentrations, thereby accelerate catalysis. However, homogeneous catalysts often face limitations in terms of their solubility in organic media and interfacial electron/mass transfer. In recent years, metal–organic frameworks (MOFs) have gained increasing attention as photocatalysts due to their high porosity, chemical stability, and synthetic tunability.<sup>23–29</sup> Especially, zirconium-based MOFs can be custom-designed for specific applications under harsh conditions,<sup>30</sup> making them potential platforms for the construction of site-isolated light-absorbing entities and single-site CO<sub>2</sub> reduction catalysts.<sup>23,28</sup> In this context, the immobilization of hydroxyl-modified porphyrinic fragments into Zr-MOF skeletons appears to be a judicious choice for the construction of potential photocatalysts for CO<sub>2</sub> reduction.<sup>31,32</sup>

While the search for reusable and stable catalysts for visible light-promoted CO<sub>2</sub> reduction continues, there is a growing gap between design and preparation that represents a critical limitation. In this study, we presented a couple of structural models in which molecular catalysts are successfully incorporated into Zr-MOFs for photocatalytic CO<sub>2</sub> reduction. One such model is an iron porphyrin-based MOF with phenolic hydroxyl modification, called **MOF-OH** (Zr<sub>6</sub>O<sub>4</sub>(OH)<sub>4</sub>(FeTCBPP-OH)<sub>3</sub>, FeTCBPP-OH = iron 5,10,15,20-tetrakis[4-(4'-carboxyphenyl)-2,6-dihydroxyphenyl]porphyrin). **MOF-OH** can be obtained through the post-synthetic modification of **MOF-OCH<sub>3</sub>** (Zr<sub>6</sub>O<sub>4</sub>(OH)<sub>4</sub>(FeTCBPP-OCH<sub>3</sub>)<sub>3</sub>, FeTCBPP-OCH<sub>3</sub> = iron 5,10,15,20-tetrakis[4-(4'-carboxyphenyl)-2,6-dimethoxyphenyl]porphyrin). Direct synthesis of **MOF-OH** through the assembly of precursors was not possible due to the higher binding affinity of hydroxyl groups on the polyphenolic porphyrinic fragments towards zirconium centers.<sup>33,34</sup> The resulting 3D microporous **MOF-OH**, with numerous local proton sources, was employed as a heterogeneous photocatalyst, demonstrating effective integration of CO<sub>2</sub> capture and reduction under visible-light irradiation. For comparison, photocatalytic CO<sub>2</sub> reduction of **MOF-OCH<sub>3</sub>** was also explored to elucidate the role of hydroxyl groups attached to the skeletons between **MOF-OH** and **MOF-OCH<sub>3</sub>**. Furthermore, a comprehensive series of experimental characterizations and density functional theory (DFT) calculations were conducted to propose a mechanism for CO<sub>2</sub> photoreduction.

## Results and discussion

### Syntheses and characterization

The solvothermal reaction of FeTCBPP-OCH<sub>3</sub>, ZrCl<sub>4</sub>, and benzoic acid in *N,N*-diethylformamide (DEF) at 120 °C for 48 h yielded dark purple cubic crystals with the framework formula of [Zr<sub>6</sub>O<sub>4</sub>(OH)<sub>4</sub>(FeTCBPP-OCH<sub>3</sub>)<sub>3</sub>] (noted as **MOF-OCH<sub>3</sub>**, Fig. 1). Furthermore, the direct assembly of the Zr<sup>4+</sup> centres and the

FeTCBPP-OH fragments under similar conditions was unsuccessful. Fortunately, **MOF-OH** ([Zr<sub>6</sub>O<sub>4</sub>(OH)<sub>4</sub>(FeTCBPP-OH)<sub>3</sub>]) was achieved by post-synthetic modification of **MOF-OCH<sub>3</sub>** with demethylation reaction. There are two types of cages constructed by Zr<sub>6</sub>O<sub>4</sub>(OH)<sub>4</sub> clusters (Zr<sub>6</sub>, Fig. S1a, ESI†) and FeTCBPP-OCH<sub>3</sub> fragments (Fig. S1b, ESI†) in **MOF-OCH<sub>3</sub>**: (i) large cubic cages (Fig. S1c, ESI†), in which each vertex is occupied by a typical 12-connected Zr<sub>6</sub> cluster, and each face is a 4-connected FeTCBPP-OCH<sub>3</sub>, and (ii) small cages (Fig. S1d, ESI†), which consist of two Zr<sub>6</sub> clusters on the axial sites and four FeTCBPP-OCH<sub>3</sub> on the longitude positions. Thus, the expected (4,12)-connected *ftw* topology is formed when the Zr<sub>6</sub> units are considered as 12-c nodes and the organic linkers as 4-c nodes. Furthermore, the space of an individual net is large enough to result in a two-fold interpenetration in **MOF-OCH<sub>3</sub>** (Fig. S1e and f, ESI†). **MOF-OH** is conformationally identical to **MOF-OCH<sub>3</sub>**, except that part of the methoxy groups of the FeTCBPP-OCH<sub>3</sub> fragments was demethylated in **MOF-OH**. After demethylation, the microenvironment was changed, resulting in a couple of structural models with the introduction of iron tetraphenylporphyrin fragments into Zr-MOFs for a potential study on photocatalytic CO<sub>2</sub> reduction.

After the analysis of mass spectra and <sup>1</sup>H NMR spectra of **MOF-OH** and **MOF-OCH<sub>3</sub>** (Fig. S2 and S3, ESI†), it was observed that FeTCBPP-OCH<sub>3</sub> was partially converted to FeTCBPP-OH in **MOF-OH**. According to quantitative calculations from <sup>1</sup>H NMR results, approximately 62.5% of the methoxy groups in **MOF-OCH<sub>3</sub>** were converted to hydroxyl groups. The powder X-ray diffraction (PXRD) patterns of **MOF-OCH<sub>3</sub>** and **MOF-OH** matched well with the simulated ones, which confirmed the purities of these two MOFs (Fig. 2a). The porosities of these MOFs were confirmed by N<sub>2</sub> adsorption at 77 K (Fig. 2b). **MOF-OCH<sub>3</sub>** and **MOF-OH** exhibited type I isotherms, due to the micropore nature of the interpenetrated structures. The Brunauer–Emmett–Teller (BET) surface areas were 1613 and 493 m<sup>2</sup> g<sup>−1</sup> for **MOF-OCH<sub>3</sub>** and **MOF-OH**, respectively. The pore size and BET surface area of **MOF-OH** were reduced after the post-synthetic modification (Fig. S4, ESI†), which could be attributed to capillary-force-driven pore collapsing during

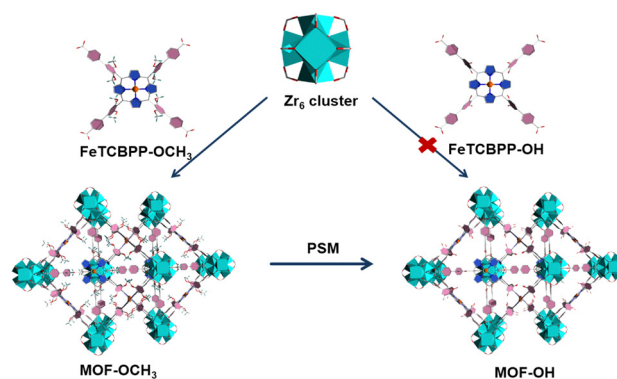


Fig. 1 Schematic diagram for the preparation of **MOF-OCH<sub>3</sub>** and **MOF-OH**. Colour codes: ZrO<sub>8</sub> polyhedron, cyan polyhedra; C, gray; O, red; N, blue; Fe, orange; H, olive or omitted for clarity.

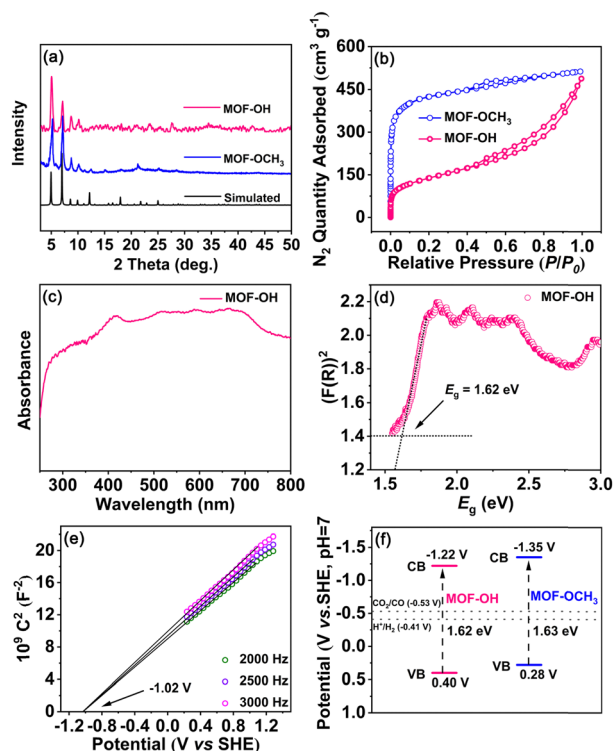


Fig. 2 (a) PXRD patterns and (b)  $N_2$  isotherms at 77 K of **MOF-OH** and **MOF-OCH<sub>3</sub>**, respectively. (c) UV-vis spectrum and (d) diffuse reflectance spectrum via K–M transformation of **MOF-OH**, (e) Mott–Schottky plots of the as-prepared **MOF-OH** electrode, and (f) calculated redox potentials of **MOF-OH** and **MOF-OCH<sub>3</sub>**, respectively.

desorption.<sup>35,36</sup> This result can be assigned to the preparation conditions of **MOF-OH**, which was synthesized from **MOF-OCH<sub>3</sub>** through  $BBr_3$  cleavage ether reaction and post-treatment with water. Thermal-gravimetric analysis (TGA) confirmed that both **MOF-OH** and **MOF-OCH<sub>3</sub>** exhibited excellent thermal stabilities, and no obvious weight loss was observed until 400 °C (Fig. S5, ESI†).

### Thermodynamic feasibility for CO<sub>2</sub> reduction

In the UV-vis spectra of **MOF-OH** and **MOF-OCH<sub>3</sub>** (Fig. 2c and Fig. S6, ESI†), a broad and strong absorption was observed in the range from 250 to 800 nm, which inherits the feature of the porphyrin fragments. These results perhaps allowed for promoting the electrons of **MOF-OH** and **MOF-OCH<sub>3</sub>** to an excited state upon visible-light irradiation.<sup>37</sup> The band gap ( $E_g$ ) was tested by fitting the Tauc function to the K–M absorbance above the Urbach tail.<sup>38</sup> Accordingly, the  $E_g$  values of **MOF-OH** and **MOF-OCH<sub>3</sub>** can be estimated to  $\sim 1.62$  and  $\sim 1.63$  eV (Fig. 2d and Fig. S7, ESI†), indicating the semiconductivities of these two materials. In addition, Mott–Schottky measurements of **MOF-OH** and **MOF-OCH<sub>3</sub>** were conducted at frequencies of 2000, 2500, and 3000 Hz (Fig. 2e and Fig. S8, ESI†), respectively. Furthermore, the conduction-band (CB) position was estimated by measuring the flatband potential ( $E_{fb}$ ) via Mott–Schottky plots. The positive slope of the plots indicates the n-type semiconductors of **MOF-OH** and **MOF-OCH<sub>3</sub>**,<sup>39</sup> and  $E_{fb}$  were evaluated to be approx.  $-1.02$  and  $-1.15$  V vs. SHE, respectively.

Since  $E_{fb}$  of n-type semiconductors was considered to be  $\sim 0.2$  V more negative than the CB minima,<sup>40</sup> the CB of **MOF-OH** and **MOF-OCH<sub>3</sub>** were estimated to be approx.  $-1.22$  and  $-1.35$  V vs. SHE (Fig. 2f), which is more negative than the redox potentials of  $CO/CO_2$  ( $-0.53$  V vs. SHE, pH 7).<sup>41</sup> Thus, **MOF-OH** and **MOF-OCH<sub>3</sub>** possess strong thermodynamic driving forces to realize  $CO_2$  reduction.

### Catalytic performance in overall CO<sub>2</sub> photoreduction

In light of the good semiconductor characteristics and excellent stabilities of Zr-MOFs, **MOF-OH** and **MOF-OCH<sub>3</sub>** were utilized as photocatalysts for  $CO_2$  reduction. Photocatalytic reduction of  $CO_2$  over **MOF-OH** was conducted with 0.025 M BIH and 3 vol% 2,2,2-trifluoroethanol (TFE) in a 5 mL acetonitrile (MeCN) as solvent under an LED lamp irradiation ( $\lambda = 420$  nm). Remarkably, **MOF-OH** exhibited significant photocatalytic  $CO_2$  reduction activity. The yield of CO increased with time and was up to  $26.8$  mmol  $g^{-1}$  at 72 h (Fig. 3a), which was much higher than those of the homogeneous molecular systems.<sup>42</sup> In addition, only a minor amount of  $H_2$  was observed by gas chromatography. No other products could be detected in either the gas or liquid phases, suggesting that **MOF-OH** possessed a high CO selectivity of 93% toward the  $CO_2$  conversion. As a comparison, the performance of **MOF-OCH<sub>3</sub>** was also carried out under the same conditions. The photocatalytic activity of **MOF-OH** was much higher than that of **MOF-OCH<sub>3</sub>**, which suggested the critical role of the phenol substituents on the phenyl rings in orienting the photocatalysis towards  $CO_2$  reduction. Furthermore, no CO was detected without **MOF-OH** (Fig. 3b), demonstrating the crucial role in the reaction. In the absence of BIH, no CO was produced, proving that BIH was essential as a sacrificial electron donor for  $CO_2$  reduction.<sup>43</sup> A decrease in CO production was observed without TFE, suggesting that proper weak Brønsted acids significantly improved the catalytic process.<sup>44,45</sup> Moreover, no CO was produced when the parallel

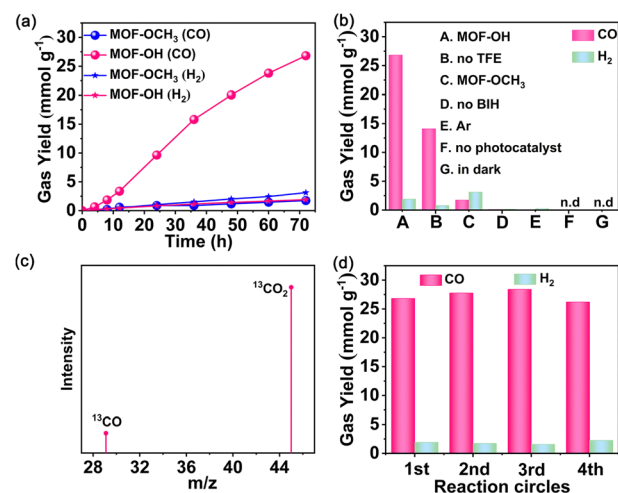


Fig. 3 Visible-light-driven  $CO_2$  reduction performance of **MOF-OH** and **MOF-OCH<sub>3</sub>**: (a) time-dependent  $CO/H_2$  yields over **MOF-OH** (pink) and **MOF-OCH<sub>3</sub>** (blue), (b) the yields of  $CO/H_2$  under different conditions, (c) mass spectrum of produced  $^{13}CO$  via isotope  $^{13}CO_2$  reduction under visible light, and (d) the yields of  $CO/H_2$  over **MOF-OH** of four runs.



reaction was carried out in the dark, revealing a truly photocatalytic behaviour. To confirm the origin of CO, Ar as a reactant was added to the reaction system instead of CO<sub>2</sub> under a similar condition. However, no CO was detected.

In addition, isotope labelling experiments were performed by using <sup>13</sup>CO<sub>2</sub> under the same conditions (Fig. 3c). A clear signal at an *m/z* ratio of 29 was observed that corresponding to <sup>13</sup>CO, which verified the source of CO. No obvious change in CO production occurred during the four runs, demonstrated the stability of **MOF-OH** (Fig. 3d). The PXRD patterns further manifested that the skeleton of **MOF-OH** was retained after CO<sub>2</sub> reduction (Fig. S9, ESI†).

### Mechanism study

The charge separation efficiency is considered to be of paramount importance for determining the photocatalytic activity.<sup>46</sup> The photoelectrochemical properties were performed with the combination of transient photocurrent measurements and electrochemical impedance spectroscopy (EIS). Both **MOF-OCH<sub>3</sub>** and **MOF-OH** exhibited obvious photocurrent signals and demonstrated excellent reproducibility of the response intensity throughout the on-off cycles (Fig. S10a, ESI†). However, the transient photocurrent intensity of **MOF-OH** is ~3 times that of **MOF-OCH<sub>3</sub>**. In addition, the EIS spectra revealed that **MOF-OH** exhibited a smaller semicircle radius compared to **MOF-OCH<sub>3</sub>** (Fig. S10b, ESI†). These results indicated the presence of a higher separation and transfer efficiency of charge carriers in **MOF-OH**. In addition, photoluminescence (PL) spectra and time-resolved PL spectra were analysed to investigate the charge migration dynamics. The fluorescence intensity of **MOF-OH** was lower than that of **MOF-OCH<sub>3</sub>** (Fig. S11a, ESI†), indicating that the charge recombination was suppressed in **MOF-OH**. The

average lifetime of **MOF-OH** (2.32 ns) was shorter compared to **MOF-OCH<sub>3</sub>** (4.46 ns) (Fig. S11b, ESI†), suggesting that the efficient electron-hole pairs separation in **MOF-OH** and therefore more favourable for photocatalytic CO<sub>2</sub> reduction.<sup>47,48</sup>

To further investigate the rapid charge separation of photocatalysts, we recorded the femtosecond time-resolved transient absorption (fs-TA) spectra that is a powerful tool for tracking carrier dynamics in nanosystems in real time. For the measurements, a pump-probe scheme with visible-light pumping and white-light continuous probing was used. The fs-TA spectra of **MOF-OH** and **MOF-OCH<sub>3</sub>** were recorded in the wavelength range of 450–750 nm under the excitation with a 400 nm laser pulse (Fig. 4a and b). For **MOF-OH**, pulsed laser excitation resulted in a bleaching signal in 500–530 nm, which was a ground-state bleaching. The absorption signal in the excited state appeared at 530–750 nm. By probing the absorption intensity at  $\lambda = 700$  nm after band edge excitation, the kinetic curves for **MOF-OH** and **MOF-OCH<sub>3</sub>** were shown in Fig. 4c and d. Most importantly, the average lifetime ( $\tau_{\text{ave}}$ ) of **MOF-OH** (94.0 ± 8.1 ps) was shorter than that of **MOF-OCH<sub>3</sub>** (225.6 ± 15.5 ps). The fast component may be attributed to fast electron transfer from the conduction-band minimum of the MOF to the trap state, suggesting that the accelerated TA decay kinetics suppressed electron-hole binding. This result was also consistent with the transient photocurrent measurements and EIS results.

To investigate the conversion pathway and mechanism of CO<sub>2</sub> in **MOF-OH**, the intermediates on the surface of the photocatalysts were analysed by using *in situ* attenuated total reflection Fourier transform infrared spectroscopy (ATR-FTIR). As shown in Fig. 4e, the carbonate species, *i.e.* monodentate carbonate (m-CO<sub>3</sub><sup>2-</sup>, at 1345 cm<sup>-1</sup>), bidentate carbonate (b-CO<sub>3</sub><sup>2-</sup>, at 1598 and 1282 cm<sup>-1</sup>),<sup>49</sup> and bicarbonate (c-CO<sub>3</sub><sup>2-</sup>, at

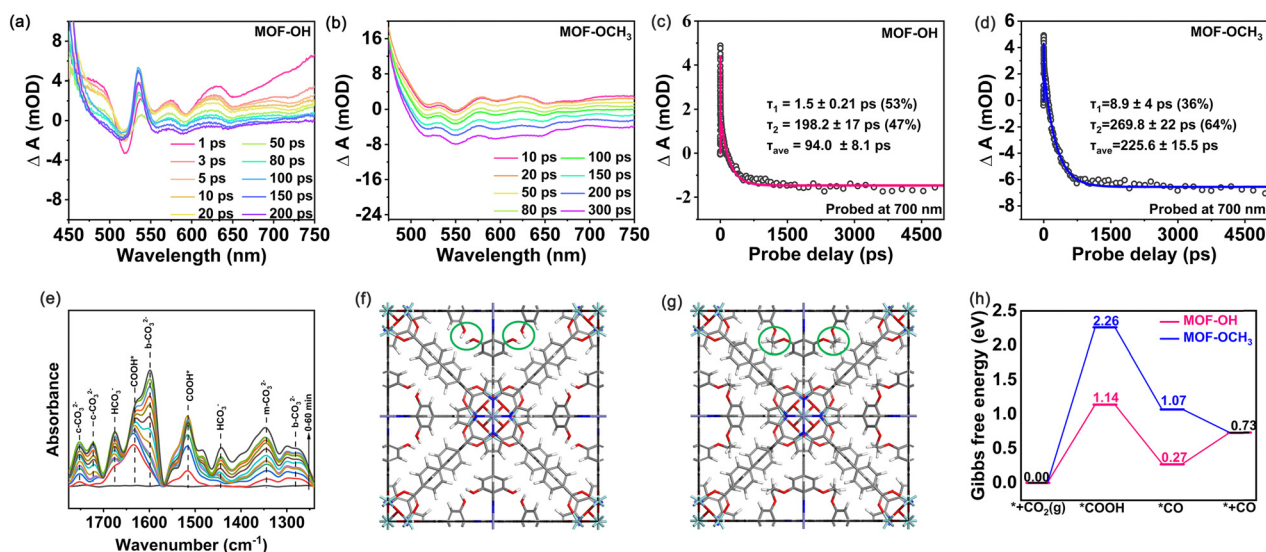
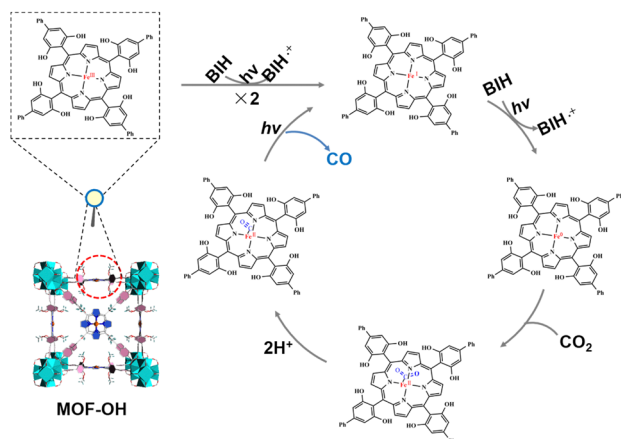


Fig. 4 (a) and (b) fs-TA data of **MOF-OH** and **MOF-OCH<sub>3</sub>** excited at 400 nm showing the temporal changes at different time constants. (c) and (d) Representative TA kinetics of **MOF-OH** and **MOF-OCH<sub>3</sub>** taken at the probing wavelength of 700 nm. (e) *In situ* ATR-FTIR measurement using **MOF-OH** as a catalyst in the presence of CO<sub>2</sub> and H<sub>2</sub>O vapor under visible light irradiation (Xe lamp,  $\lambda > 420$  nm). Optimized structural models of (f) **MOF-OH** and (g) **MOF-OCH<sub>3</sub>**. The green circles indicated the hydroxy and methoxy. (h) Gibbs free energy diagrams for CO<sub>2</sub> reduction on **MOF-OH** and **MOF-OCH<sub>3</sub>**, respectively.



**Scheme 1** Proposed mechanism for the overall  $\text{CO}_2$  photoreduction of **MOF-OH**.

1752 and  $1721\text{ cm}^{-1}$ ) were identified. Additionally, the peaks at  $1676$  and  $1444\text{ cm}^{-1}$  can be assigned to asymmetric stretching of  $^*\text{HCO}_3^-$  and symmetric stretching of  $^*\text{HCO}_3^-$ , respectively.<sup>50</sup> The peaks at  $1631$ ,  $1515\text{ cm}^{-1}$  emerged, which were attributed to the formation of  $\text{COOH}^*$ ,<sup>49,51</sup> a critical intermediate during the photoreduction of  $\text{CO}_2$  to  $\text{CO}$ .

Furthermore, DFT calculations were carried out to investigate the mechanism of  $\text{CO}_2$  reduction to  $\text{CO}$  over **MOF-OH** and **MOF-OCH<sub>3</sub>** (computational details can be found in the ESI†). The fully optimized geometric models of **MOF-OH** and **MOF-OCH<sub>3</sub>** were shown in Fig. 4f and g, where their difference of building groups was marked in green circles. The central Fe atom of the porphyrin ring was well-accepted to be the active site for  $\text{CO}_2$  reduction, which was consistent with previous reports.<sup>52,53</sup> The second coordination spheres of polyhydroxy groups offer a high local concentration of protons, which enhanced the photocatalytic efficiencies in terms of both rate constant and catalytic selectivity. To further understand the better catalytic performance of **MOF-OH** than that of **MOF-OCH<sub>3</sub>**, the Gibbs free energy diagrams for  $\text{CO}_2$  reduction to  $\text{CO}$  were systematically considered and explored (Fig. 4h). The  $\text{CO}_2$  reduction starts with forming  $^*\text{C-Fe}$  bonding at the active site and the subsequent proton-coupled electron transfer process to produce  $^*\text{COOH}$  intermediate. The computed  $\Delta G$  values for this elementary reaction on **MOF-OH** and **MOF-OCH<sub>3</sub>** were  $1.14$  and  $2.26\text{ eV}$ , respectively. Subsequently, the  $^*\text{COOH}$  intermediate was further hydrogenated to generate  $^*\text{CO}$  intermediate. This process is exothermic in the Gibbs free energy diagram. The formed  $^*\text{CO}$  intermediate on **MOF-OH** can easily release the  $\text{CO}$  gas by overcoming a small barrier by  $0.46\text{ eV}$ . These results confirmed the better catalytic activity of **MOF-OH**, which further explained the much higher  $\text{CO}$  yield of **MOF-OH** than that of **MOF-OCH<sub>3</sub>**.

On the basis of the above investigations, we proposed the mechanism of overall  $\text{CO}_2$  photoreduction over **MOF-OH** (Scheme 1).  $\text{CO}_2$  was first complexed with the triply reduced  $\text{Fe}^0$  species (forming  $\text{Fe}^0\text{CO}_2$ ), which after protonation, produced a  $\text{Fe}^{\text{II}}\text{CO}$  intermediate, which is stabilized by internal

hydrogen bonding.<sup>54,55</sup> The release of  $\text{CO}$  requires the breaking of the  $\text{C-O}$  bond and therefore an additional electron. In addition, it was noted that the electron-rich  $\text{Fe}^0$  species can react with  $\text{H}^+$  to generate  $\text{Fe}^{\text{II}}$  and the unrequired byproduct  $\text{H}_2$ , although it remained a minor pathway in optimized conditions. On the other hand, a high concentration of  $\text{Fe}^0$  active species in solution that would ensue from highly efficient electron transfers from the sensitizer can also support  $\text{H}_2$  evolution.

## Conclusions

In conclusion, we achieved the production of **MOF-OH** through a demethylation-driven post-synthetic modification process. This involved modifying the methoxy groups of the **FeTCBPP-OCH<sub>3</sub>** fragments in **MOF-OCH<sub>3</sub>**. The yield of  $\text{CO}$  reached an impressive  $26.8\text{ mmol g}^{-1}$  after 72 hours using **MOF-OH** as the photocatalyst for  $\text{CO}_2$  reduction, even without any photosensitizer. This yield was significantly higher than that achieved with **MOF-OCH<sub>3</sub>**. Comprehensive studies on the kinetic mechanism revealed that the exceptional photocatalytic performance of **MOF-OH** can be primarily attributed to the iron porphyrin ligand with phenolic hydroxyl groups. These groups successfully immobilized the catalytic centre within the MOFs, facilitating ultrafast electron migration and efficient charge separation. Furthermore, the introduction of phenolic hydroxyl groups resulted in a high concentration of local protons, greatly enhancing the photocatalytic efficiencies. Additionally, DFT calculations demonstrated that **MOF-OH** can easily release  $\text{CO}$  gas by overcoming a small potential barrier in the formed  $^*\text{CO}$  intermediate, compared to **MOF-OCH<sub>3</sub>**. This work not only provides a solid foundation for the accurate design of MOF photocatalysts at the molecular level but also presents successful MOF models that can be used to investigate the relationship between structures and photocatalytic performances. These findings strongly emphasize the need for further studies to explore the multifunctional coordination sphere of MOF photocatalysts. Moreover, ongoing investigations in our laboratory aim to delve into the design and performance of the pore microenvironment.

## Author contributions

Xue Zhao: validation, formal analysis, investigation, data curation, writing – original draft. Chang-Yan Zhu: data curation, writing – original draft. Jun-Sheng Qin: conceptualization, funding acquisition, project administration. Heng Rao: conceptualization, funding acquisition. Dong-Ying Du: conceptualization, validation, writing – review & editing. Min Zhang: data curation, conceptualization. Ping She: conceptualization, funding acquisition. Li Li: conceptualization. Zhong-Min Su: project administration.

## Conflicts of interest

The authors declare no competing financial interest.

## Acknowledgements

This work was financially supported in part by the National Natural Science Foundation of China (Grant No. 21901084, 21905106, 22301099 and 22279041), the Natural Science Foundation of Jilin Province (No. SKL202302017), the National Key Research and Development Program of China (No. 2022YFC2105800) and the 111 Project (B17020).

## References

- 1 T. Kong, Y. Jiang and Y. Xiong, Photocatalytic CO<sub>2</sub> conversion: What can we learn from conventional CO<sub>x</sub> hydrogenation?, *Chem. Soc. Rev.*, 2020, **49**, 6579–6591.
- 2 T. Nakajima, Y. Tamaki, K. Ueno, E. Kato, T. Nishikawa, K. Ohkubo, Y. Yamazaki, T. Morimoto and O. Ishitani, Photocatalytic Reduction of Low Concentration of CO<sub>2</sub>, *J. Am. Chem. Soc.*, 2016, **138**, 13818–13821.
- 3 J. S. Qin, S. Yuan, L. Zhang, B. Li, D. Y. Du, N. Huang, W. Guan, H. F. Drake, J. Pang, Y. Q. Lan, A. Alsalmeh and H. C. Zhou, Creating Well-Defined Hexabenzocoronene in Zirconium Metal-Organic Framework by Postsynthetic Annulation, *J. Am. Chem. Soc.*, 2019, **141**, 2054–2060.
- 4 J. Tian, R. Han, Q. Guo, Z. Zhao and N. Sha, Direct Conversion of CO<sub>2</sub> into Hydrocarbon Solar Fuels by a Synergistic Photothermal Catalysis, *Catalysts*, 2022, **12**, 612.
- 5 K. Li, X. An, K. H. Park, M. Khraisheh and J. Tang, A critical review of CO<sub>2</sub> photoconversion: Catalysts and reactors, *Catal. Today*, 2014, **224**, 3–12.
- 6 H. Yuan, B. Cheng, J. Lei, L. Jiang and Z. Han, Promoting photocatalytic CO<sub>2</sub> reduction with a molecular copper purpurin chromophore, *Nat. Commun.*, 2021, **12**, 1835.
- 7 F. D. Bobbink and P. J. Dyson, Synthesis of carbonates and related compounds incorporating CO<sub>2</sub> using ionic liquid-type catalysts: State-of-the-art and beyond, *J. Catal.*, 2016, **343**, 52–61.
- 8 S.-H. Wang, F. Khurshid, P.-Z. Chen, Y.-R. Lai, C.-W. Cai, P.-W. Chung, M. Hayashi, R.-J. Jeng, S.-P. Rwei and L. Wang, Solution-Processable Naphthalene Diimide-Based Conjugated Polymers as Organocatalysts for Photocatalytic CO<sub>2</sub> Reaction with Extremely Stable Catalytic Activity for Over 330 Hours, *Chem. Mater.*, 2022, **34**, 4955–4963.
- 9 S. Kreft, D. Wei, H. Junge and M. Beller, Recent advances on TiO<sub>2</sub>-based photocatalytic CO<sub>2</sub> reduction, *EnergyChem*, 2020, **2**, 100044.
- 10 Ș. Neațu, J. Maciá-Agulló and H. Garcia, Solar Light Photocatalytic CO<sub>2</sub> Reduction: General Considerations and Selected Bench-Mark Photocatalysts, *Int. J. Mol. Sci.*, 2014, **15**, 5246–5262.
- 11 A. Muthuperiyanyagam, A. G. Nabi, Q. Zhao, R. Aman Ur and D. D. Tommaso, Adsorption, activation, and conversion of carbon dioxide on small copper-tin nanoclusters, *Phys. Chem. Chem. Phys.*, 2023, **25**, 13429–13441.
- 12 A. Vidal-López, S. Posada-Pérez, M. Solà and A. Poater, Au Single Metal Atom for Carbon Dioxide Reduction Reaction, *Chemistry*, 2023, **5**, 1395–1406.
- 13 W. Deng, P. Zhang, B. Seger and J. Gong, Unraveling the rate-limiting step of two-electron transfer electrochemical reduction of carbon dioxide, *Nat. Commun.*, 2022, **13**, 803.
- 14 J. Kim and E. E. Kwon, Photoconversion of carbon dioxide into fuels using semiconductors, *J. CO<sub>2</sub> Util.*, 2019, **33**, 72–82.
- 15 J. W. Wang, F. Ma, T. Jin, P. He, Z. M. Luo, S. Kupfer, M. Karnahl, F. Zhao, Z. Xu, T. Jin, T. Lian, Y. L. Huang, L. Jiang, L. Z. Fu, G. Ouyang and X. Y. Yi, Homoleptic Al(III) Photosensitizers for Durable CO<sub>2</sub> Photoreduction, *J. Am. Chem. Soc.*, 2023, **145**, 676–688.
- 16 H. Takeda, K. Ohashi, A. Sekine and O. Ishitani, Photocatalytic CO<sub>2</sub> Reduction Using Cu(I) Photosensitizers with a Fe(II) Catalyst, *J. Am. Chem. Soc.*, 2016, **138**, 4354–4357.
- 17 H. Rao, C. H. Lim, J. Bonin, G. M. Miyake and M. Robert, Visible-Light-Driven Conversion of CO<sub>2</sub> to CH<sub>4</sub> with an Organic Sensitizer and an Iron Porphyrin Catalyst, *J. Am. Chem. Soc.*, 2018, **140**, 17830–17834.
- 18 H. Rao, L. C. Schmidt, J. Bonin and M. Robert, Visible-light-driven methane formation from CO<sub>2</sub> with a molecular iron catalyst, *Nature*, 2017, **548**, 74–77.
- 19 R. Wan, D. G. Ha, J. H. Dou, W. S. Lee, T. Chen, J. J. Oppenheim, J. Li, W. A. Tisdale and M. Dinca, Dipole-mediated exciton management strategy enabled by reticular chemistry, *Chem. Sci.*, 2022, **13**, 10792–10797.
- 20 C. Costentin, S. Drouet, M. Robert and J.-M. Savéant, A Local Proton Source Enhances CO<sub>2</sub> Electroreduction to CO by a Molecular Fe Catalyst, *Science*, 2012, **338**, 90–94.
- 21 C. Costentin, G. Passard, M. Robert and J. M. Saveant, Pendant acid-base groups in molecular catalysts: H-bond promoters or proton relays? Mechanisms of the conversion of CO<sub>2</sub> to CO by electrogenerated iron(0)porphyrins bearing prepositioned phenol functionalities, *J. Am. Chem. Soc.*, 2014, **136**, 11821–11829.
- 22 C. Costentin, G. Passard, M. Robert and J. M. Saveant, Ultraefficient homogeneous catalyst for the CO<sub>2</sub>-to-CO electrochemical conversion, *Proc. Natl. Acad. Sci. U. S. A.*, 2014, **111**, 14990–14994.
- 23 Z. B. Fang, T. T. Liu, J. Liu, S. Jin, X. P. Wu, X. Q. Gong, K. Wang, Q. Yin, T. F. Liu, R. Cao and H. C. Zhou, Boosting Interfacial Charge-Transfer Kinetics for Efficient Overall CO<sub>2</sub> Photoreduction via Rational Design of Coordination Spheres on Metal-Organic Frameworks, *J. Am. Chem. Soc.*, 2020, **142**, 12515–12523.
- 24 X.-H. Liang, A.-X. Yu, X.-J. Bo, D.-Y. Du and Z.-M. Su, Metal/covalent-organic frameworks-based electrochemical sensors for the detection of ascorbic acid, dopamine and uric acid, *Coord. Chem. Rev.*, 2023, **497**, 215427.
- 25 G. Y. Qiao, D. Guan, S. Yuan, H. Rao, X. Chen, J. A. Wang, J. S. Qin, J. J. Xu and J. Yu, Perovskite Quantum Dots Encapsulated in a Mesoporous Metal-Organic Framework as Synergistic Photocathode Materials, *J. Am. Chem. Soc.*, 2021, **143**, 14253–14260.
- 26 S. Kampouri, M. Zhang, T. Chen, J. J. Oppenheim, A. C. Brown, M. T. Payne, J. L. Andrews, J. Sun and M. Dinca, Pyrogallate-Based Metal-Organic Framework with



- a Two-Dimensional Secondary Building Unit, *Angew. Chem., Int. Ed.*, 2022, **61**, e202213960.
- 27 A. Iliescu, J. L. Andrews, J. J. Oppenheim and M. Dinca, A Solid Zn-Ion Conductor from an All-Zinc Metal-Organic Framework Replete with Mobile  $\text{Zn}^{2+}$  Cations, *J. Am. Chem. Soc.*, 2023, **145**, 25962–25965.
  - 28 H. Q. Xu, J. Hu, D. Wang, Z. Li, Q. Zhang, Y. Luo, S. H. Yu and H. L. Jiang, Visible-Light Photoreduction of  $\text{CO}_2$  in a Metal-Organic Framework: Boosting Electron-Hole Separation via Electron Trap States, *J. Am. Chem. Soc.*, 2015, **137**, 13440–13443.
  - 29 L. Feng, J. Pang, P. She, J. L. Li, J. S. Qin, D. Y. Du and H. C. Zhou, Metal-Organic Frameworks Based on Group 3 and 4 Metals, *Adv. Mater.*, 2020, **32**, e2004414.
  - 30 G. Y. Qiao, S. Yuan, J. Pang, H. Rao, C. T. Lollar, D. Dang, J. S. Qin, H. C. Zhou and J. Yu, Functionalization of Zirconium-Based Metal-Organic Layers with Tailored Pore Environments for Heterogeneous Catalysis, *Angew. Chem., Int. Ed.*, 2020, **59**, 18224–18228.
  - 31 M. E. Kosal, J.-H. Chou, S. R. Wilson and K. S. Suslick, A functional zeolite analogue assembled from metalloporphyrins, *Nat. Mater.*, 2002, **1**, 118–121.
  - 32 D. Feng, Z. Y. Gu, J. R. Li, H. L. Jiang, Z. Wei and H. C. Zhou, Zirconium-metalloporphyrin PCN-222: mesoporous metal-organic frameworks with ultrahigh stability as biomimetic catalysts, *Angew. Chem., Int. Ed.*, 2012, **51**, 10307–10310.
  - 33 J. Aguilera-Sigalat, A. Fox-Charles and D. Bradshaw, Direct photo-hydroxylation of the Zr-based framework UiO-66, *Chem. Commun.*, 2014, **50**, 15453–15456.
  - 34 F. M. Al-Sogair, B. P. Operschall, A. Sigel, H. Sigel, J. Schnabl and R. K. Sigel, Probing the metal-ion-binding strength of the hydroxyl group, *Chem. Rev.*, 2011, **111**, 4964–5003.
  - 35 J. E. Mondloch, M. J. Katz, N. Planas, D. Semrouni, L. Gagliardi, J. T. Hupp and O. K. Farha, Are  $\text{Zr}_6$ -based MOFs water stable? Linker hydrolysis vs. capillary-force-driven channel collapse, *Chem. Commun.*, 2014, **50**, 8944–8946.
  - 36 T. Y. Luo, S. Park, T. H. Chen, Prerna, R. Patel, X. Li, J. Ilja Siepmann, S. Caratzoulas, Z. Xia and M. Tsapatsis, Simultaneously Enhanced Hydrophilicity and Stability of a Metal-Organic Framework via Post-Synthetic Modification for Water Vapor Sorption/Desorption, *Angew. Chem., Int. Ed.*, 2022, **61**, e202209034.
  - 37 J. Jin, Porphyrin-based metal-organic framework catalysts for photoreduction of  $\text{CO}_2$ : understanding the effect of node connectivity and linker metalation on activity, *New J. Chem.*, 2020, **44**, 15362–15368.
  - 38 N. Sharma, K. Prabakar, S. Ilango, S. Dash and A. K. Tyagi, Optical band-gap and associated Urbach energy tails in defected AlN thin films grown by ion beam sputter deposition: Effect of assisted ion energy, *Adv. Mater. Process.*, 2021, **2**, 342–346.
  - 39 Y. Gao, J. Duan, X. Zhai, F. Guan, X. Wang, J. Zhang and B. Hou, Photocatalytic Degradation and Antibacterial Properties of  $\text{Fe}^{3+}$ -Doped Alkalized Carbon Nitride, *Nanomaterials*, 2020, **10**, 1751.
  - 40 L. Shi, P. Li, W. Zhou, T. Wang, K. Chang, H. Zhang, T. Kako, G. Liu and J. Ye, n-type boron phosphide as a highly stable, metal-free, visible-light-active photocatalyst for hydrogen evolution, *Nano Energy*, 2016, **28**, 158–163.
  - 41 Y. Cao, Q. Chen, C. Shen and L. He, Polyoxometalate-Based Catalysts for  $\text{CO}_2$  Conversion, *Molecules*, 2019, **24**, 2069.
  - 42 J. Bonin, M. Robert and M. Routier, Selective and Efficient Photocatalytic  $\text{CO}_2$  Reduction to CO Using Visible Light and an Iron-Based Homogeneous Catalyst, *J. Am. Chem. Soc.*, 2014, **136**, 16768–16771.
  - 43 S. Choi, W. J. Jung, K. Park, S. Y. Kim, J. O. Baeg, C. H. Kim, H. J. Son, C. Pac and S. O. Kang, Rapid Exciton Migration and Amplified Funneling Effects of Multi-Porphyrin Arrays in a Re(i)/Porphyrinic MOF Hybrid for Photocatalytic  $\text{CO}_2$  Reduction, *ACS Appl. Mater. Interfaces*, 2021, **13**, 2710–2722.
  - 44 Y. Kuramochi and A. Satake, Photocatalytic  $\text{CO}_2$  Reductions Catalyzed by meso-(1,10-Phenanthroline-2-yl)-Porphyrins Having a Rhenium(i) Tricarbonyl Complex, *Chem. – Eur. J.*, 2020, **26**, 16365–16373.
  - 45 M. Lupa-Myszkowska, M. Oszejka and D. Matoga, From non-conductive MOF to proton-conducting metal-HOFs: a new class of reversible transformations induced by solvent-free mechanochemistry, *Chem. Sci.*, 2023, **14**, 14176–14181.
  - 46 J. Gu, Q. Huang, Y. Yuan, K.-H. Ye, Z. Wang and W. Mai, In situ growth of a  $\text{TiO}_2$  layer on a flexible Ti substrate targeting the interface recombination issue of  $\text{BiVO}_4$  photoanodes for efficient solar water splitting, *J. Mater. Chem. A*, 2017, **5**, 20195–20201.
  - 47 X. Gao, B. Guo, C. Guo, Q. Meng, J. Liang and J. Liu, Zirconium-Based Metal-Organic Framework for Efficient Photocatalytic Reduction of  $\text{CO}_2$  to CO: The Influence of Doped Metal Ions, *ACS Appl. Mater. Interfaces*, 2020, **12**, 24059–24065.
  - 48 R. Hariri and S. Dehghanpour, Effective visible-light  $\text{CO}_2$  photoreduction over (metallo)porphyrin-based metal-organic frameworks to achieve useful hydrocarbons, *Appl. Organomet. Chem.*, 2021, **35**, e6422.
  - 49 J. Zhou, J. Li, L. Kan, L. Zhang, Q. Huang, Y. Yan, Y. Chen, J. Liu, S. L. Li and Y. Q. Lan, Linking oxidative and reductive clusters to prepare crystalline porous catalysts for photocatalytic  $\text{CO}_2$  reduction with  $\text{H}_2\text{O}$ , *Nat. Commun.*, 2022, **13**, 4681.
  - 50 L. Ran, Z. Li, B. Ran, J. Cao, Y. Zhao, T. Shao, Y. Song, M. K. H. Leung, L. Sun and J. Hou, Engineering Single-Atom Active Sites on Covalent Organic Frameworks for Boosting  $\text{CO}_2$  Photoreduction, *J. Am. Chem. Soc.*, 2022, **144**, 17097–17109.
  - 51 Y. He, Y. Zhao, X. Wang, Z. Liu, Y. Yu and L. Li, Multiple Heteroatom-Hydrogen Bonds Bridging Electron Transport in Covalent Organic Framework-Based Supramolecular System for Photoreduction of  $\text{CO}_2$ , *Angew. Chem., Int. Ed.*, 2023, **62**, e202307160.
  - 52 L. Lin, C. Hou, X. Zhang, Y. Wang, Y. Chen and T. He, Highly efficient visible-light driven photocatalytic reduction of  $\text{CO}_2$  over g- $\text{C}_3\text{N}_4$  nanosheets/tetra(4-carboxyphenyl)porphyrin iron(III) chloride heterogeneous catalysts, *Appl. Catal., B*, 2018, **221**, 312–319.

- 53 J. Y. Chen, M. Li and R. Z. Liao, Mechanistic Insights into Photochemical CO<sub>2</sub> Reduction to CH<sub>4</sub> by a Molecular Iron-Porphyrin Catalyst, *Inorg. Chem.*, 2023, **62**, 9400–9417.
- 54 J. Bonin, A. Maurin and M. Robert, Molecular catalysis of the electrochemical and photochemical reduction of CO<sub>2</sub> with Fe and Co metal based complexes. Recent advances, *Coord. Chem. Rev.*, 2017, **334**, 184–198.
- 55 H. Rao, J. Bonin and M. Robert, Non-sensitized selective photochemical reduction of CO<sub>2</sub> to CO under visible light with an iron molecular catalyst, *Chem. Commun.*, 2017, **53**, 2830–2833.